Simulation and Analysis of Oscillating Airfoil Ice Shapes via a Fully Unsteady Collection Efficiency Approach

Myles Morelli
PhD Candidate
Politecnico di Milano & University of Glasgow
Milan, Italy

Beckett Y. Zhou
Research Scientist
TU Kaiserslautern
Kaiserslautern, Germany

Alberto Guardone
Full Professor
Politecnico di Milano
Milan, Italy

ABSTRACT

The aerodynamics associated with complex ice shapes degrades performance characteristics and handling qualities of rotorcraft. As a consequence, it generates high compensatory workloads for pilots making it difficult to fly in icing environments. Simulating rotorcraft icing is challenging as rotor blades experience flows at high Mach numbers which regularly produces difficult to predict mixed rime-glaze ice shapes. In conjunction with this, the motion of the blade during each revolution produces unsteady flow field behaviour and so unsteady ice accretion needs to be considered. A fully unsteady collection efficiency approach is hereby introduced to study the ice shapes formed on an oscillating rotor airfoil. The work focuses solely on two different test cases which produce largely different ice shapes caused entirely by different ice regimes. The ice shapes are measured and compared against icing wind tunnel experimental test data and prior calculations using a different approach for computing the ice thickness. These ice structures are then subject to analyses to assess possible performance degradation against the performance of a clean airfoil. Additionally, a computational aeroacoustic study investigates the possibility of using noise to detect different types of ice formation to help aid warning the pilot of dangerous icing conditions.

INTRODUCTION

In-flight icing is a challenging problem for aviation authorities, manufacturers, operators, and pilots alike. Rotorcrafts restricted flight envelope means that the operators standard protocol to *"deviate from course to avoid and navigate around any encountered icing conditions" (Ref. 1)* and manufacturers flight manual instructions to *"prohibit flight in freezing rain or icing conditions" (Ref. 2)* is a frequently unobtainable idealized scenario. This makes operating rotorcraft in conditions where in-flight icing is foreseeable an inherently high-risk flight situation. In the US alone since as lately as 2016, there have been multiple in-flight rotorcraft icing accidents recorded, of which many which have included fatalities (Refs. 3–9). The need to further understand the rotorcraft in-flight icing problem is clear, however, certification for flight in icing conditions is a demanding and an expensive endeavour. If rotorcraft are to have certified Full Ice Protection Systems (FIPS) to allow them to operate in known icing conditions they are required to oblige with Part 29-C of the regulatory code laid out by the European Aviation Safety Agency (EASA) and the Federal Aviation Authorities (FAA) (Refs. 10, 11). This requires rigorous testing for main and tail rotor blade anti-and de-icing protection systems, heated windscreens, and ice detection systems. Testing these ice protection systems for certification however is a non-trivial task. Data for certification can typically come from many sources including in-flight testing and experimental testing.

In-flight testing provides the ultimate source of data however it comes with a high cost and with large amounts of uncertainty as the ice shapes cannot be measured during flight (Refs. 12–14). Furthermore, flight testing requires specific meteorological conditions which cannot be controlled so the reproducibility of the test conditions and hence the ice shapes is problematic. Test rigs such as the Canadian National Research Council spray rig have been introduced to improve control over icing parameters during in-flight testing, however, they are limited to hover flight conditions (Ref. 15). Experimental tests in icing wind tunnels provide the most control over icing conditions yet the need to use model rotors introduces additional ice scaling parameters (Refs. 16, 17). Discrepancies between model and full-scale rotor ice shapes have been documented even with the use of ice scaling parameters leading to further research dealing with this issue (Ref. 18).

Presented at the Vertical Flight Society 75th Annual Forum & Technology Display, Philadelphia, Pennsylvania, May 13–16, 2019.
Copyright © 2019 by AHS - The Vertical Flight Society. All rights reserved.

The use of computational modeling to simulate ice shapes on rotor blades helps further understand the rotorcraft icing problem (Refs. 19, 20). As with so many other aerospace technologies, rotorcraft icing codes lag behind fixed-wing aircraft icing codes which have been well established for many years now. This is partly due to the additional complexities that the rotor blade introduces which results in a highly unsteady flow field. Subsequently, icing on the main rotor blade of a helicopter should be considered inherently as an unsteady problem which makes simulating the process challenging. Hence, rotorcraft icing simulations are required to include both the effect of the centrifugal force and the effect of the blade oscillations on the final ice shape. This however requires the use of high-fidelity icing codes which is computationally challenging.

A joint venture in 2010 between Bell Helicopter, The Boeing Company, Sikorsky Aircraft, Georgia Institute of Technology, and NASA set out to enhance understanding of rotorcraft icing with the development and validation of high-fidelity icing analysis tools. With the consensus that current data was insufficient for validation two main experimental initiatives were outlined: 1). A high-quality oscillating airfoil test to enhance the scarce dataset for validating the rotorcraft icing problem during pitching motion (Ref. 21) and 2). A spinning rotor test to assess the feasibility of scaling and evaluate hydrophobic and icephobic materials (Ref. 22). These experimental tests were then the basis for validation of high-fidelity computational rotorcraft icing tools (Refs. 23, 24). This work focuses on the validation of the oscillating airfoil test and uses the experimental test data from Reinert et al. (Ref. 21) and calculated ice shapes from Narducci and Reinert (Ref. 24) for ice shape comparisons.

As part of this collaboration between the US Government and industry, The Boeing Company calculated ice shapes on an oscillating airfoil (Ref. 24) and used the experimental work conducted in the NASA Icing Research Tunnel (IRT) (Ref. 21) to validate the code. The main goal of the work was to accurately calculate oscillating airfoil ice shapes and resultant performance characteristics. The analysis approach used was built on the premise that the ice shape is not a strong function of the frequency of oscillation which was supported by the similarity in ice shapes with different oscillatory frequencies. A further assumption was then made that the time history of a helicopter rotor blade pitching at 1/rev can be represented by a very slow moving blade. Accordingly, it was then assumed that only the mean angle of attack and extreme amplitudes of angle of attack are considered in a series of quasi-static icing events.

One of the main drawbacks of this method however is that it does not consider the effect of the unsteady flow field as the ice accretes. To help theoretically understand if a flow field can be considered as steady the reduced frequency is regularly used. The degree of unsteadiness of the oscillation can be expressed by the reduced frequency, defined in terms of the semi-chord, $b = c/2$ as

$$\text{Reduced Frequency, } k = \frac{\omega c}{2V_\infty} \tag{1}$$

for $0 \leq k \leq 0.05$ flow can be considered quasi-steady and for $k \geq 0.05$ flow is considered unsteady, where ω is the oscillatory frequency and V_∞ is the free stream velocity. For a rotor blade pitching 1/rev this may in certain cases be applicable, however, this is not positive for all instances.

Alternative approaches to predict ice shapes were also suggested in Ref. 24 which merits discussion. The first alternative approach suggested was an average angle of attack, however, then the airfoil does not oscillate and the simulation is considered entirely steady. The second alternative approach proposed was an averaging of ice shapes, where, a clean airfoil is iced at various static angles of attack and using weighted averages the final ice shape is computed. This also considers the unsteady oscillating airfoil to be steady and again neglects all aerodynamic characteristics and hysteresis behaviour associated with the oscillating motion of the airfoil outline in Ref. 25.

Five years later in 2015 another collaboration arose between The Boeing Company, Georgia Institute of Technology, Penn State University, and NASA, which involved much of the same personnel, and aimed to further develop and progress rotorcraft icing computational tools (Ref. 25). This study focused on coupled CFD/CSD analysis for rotorcraft in forward flight to assess the trim state of an iced rotor. Once again however this used the method to assume that the time history of an oscillating airfoil can represented by a slow-moving blade so that eventually the icing analysis can be thought of as a series of quasi-static events.

The importance of avoiding of possible icing conditions is evident thus, ice detection system have become integrally fundamental to helicopter safety. Since as recently as 2016, work has began to help develop technologies to detect ice formation through the quantification of rotor surface roughness due to ice via broadband noise measurements (Ref. 26).

FULLY UNSTEADY OSCILLATING AIRFOIL ICE SHAPE APPROACH

This research will seek to account for ice accretion on an oscillating airfoil inherently as a fully unsteady problem to aid in further developing rotorcraft icing tools. It will thus account for the iced airfoil geometry, reduced frequency, and amplitude of oscillations which are the primary factors causing dynamic stall (Ref. 27). This will be done using the process shown in Fig. 1 where the collection efficiency on the airfoil over a full period of oscillation will be calculated. In doing so the impingement limits and distribution of supercooled water droplets will fully take into account any possible unsteady aerodynamic flowfield effects. This will be ensured so that at every unsteady aerodynamic pseudo time-step at which the airfoil oscillates, there will be a cloud front of supercooled water droplets impacting on the airfoil. The collection efficiency can then be calculated after a full oscillation of the airfoil once it passes through the cloud. This information will then be passed onto an icing solver which, using ice accretion laws governed by the meteorological conditions during flight,

computes the newly formed ice shape. This process can then be iteratively solved in a multi-step process for a given length of ice accretion. In this approach there is no assumption of steady or quasi-steady flow even whilst $0 \leq k \leq 0.05$.

Based on the present approach an example scenario shown in Fig. 2 displays how cloud fronts containing supercooled water droplets moving in an unsteady flow field impact on an oscillating airfoil at angles of attack, $\alpha = 5^\circ \pm 6^\circ$. It shows how at different instances in time as the airfoils oscillates the dynamic pressure changes affecting the droplet trajectories. This dynamic behaviour cannot be captured whilst considering ice accretion over an oscillating airfoil as a series of quasi-static events in time. With this established, the collection efficiency takes into account all unsteady aerodynamic effects.

EXPERIMENTAL TEST CASES

The computations of the oscillating airfoil ice shapes will be compared against both experimental work and other computational in-flight icing codes. Thanks to the experimental in-flight icing tests which took place in the NASA Glenn IRT to help improve the scarce data-set of oscillating airfoils numerous different test cases have been identified. The experimental work from Rienert et al. (Ref. 21) has been used for verification of this method and the computations from Narducci and Rienert are shown for code comparisons using their IceMaker software (Ref. 24).

These test cases assess the effect of the flow field on the ice shapes, the meteorological conditions which are inherently the driver causing icing, and the length of time when exposed to icing conditions. All the variants in these test cases have been considered and simulated, nevertheless, for simplification this paper only focuses on the effect of the Liquid Water Content (LWC) on the final ice shapes and thus test case run numbers 36 and 61 have been used within this paper for analyses. The operating conditions from these test cases used for examination can be found in Table. 1.

Table 1. Test cases chosen for examination[a].

Test Case Number	Air Speed (m/s)	α (°)	LWC (g/m^3)	Time (sec)
Run 36	77	5 ± 6	0.5	600
Run 61	77	5 ± 6	1.0	600

[a]Taken from Rienert et al. (Ref. 21)

These operating conditions represent an airfoil at low flight speed and at a low mean angle of attack with significant amplitudes of oscillations. The length of time operating in icing conditions is long enough to expect significant ice accretion such that it could have severely damaging effects on the airfoils performance. The Mean Volume Diameter (MVD) of the water droplets within these cases is constant at 22 μm and is of a typical value for many icing experiments. Two different oscillating frequencies were discussed at which a conventional helicopter rotor blade would pitch per revolution, one a high-frequency oscillation at 5.8 Hz and the other a low-frequency oscillation at 2.8Hz. Results showed that the effect of the rate of oscillation was minimal on the final ice shape and for this reason, the test case with the higher rate of oscillation was chosen as it produces greater values of reduced frequency related to unsteady flow. The effect of the rate of oscillation on the ice shapes is, however, a parameter that will be considered at a later date. One of the most intriguing conditions from the experimental tests is the outside air temperature (OAT) which is at -14 °C. The OAT is representative classically of mixed rime-glaze ice accretion which can during extensive ice formation lead to the formation of symmetrical double-horn structures. These ice structures are renowned for being demanding to simulate and require an accurate ice accretion model to account for the heat diffusion within the ice layer and mass transfer from glaze to rime ice cells.

The experimental tests consisted of an untwisted Sikorsky SC2110 wing designed by Sikorsky/Lednicer and Owen as a rotorcraft airfoil and is undergoing pitch oscillation. The wing dimension has a 0.381m chord and stretches from the floor to the ceiling of the wind tunnel. The airfoil has a maximum thickness at 9.9% at 37.7% chord and has a maximum chamber of 1.9% at 15.7% chord. Work from Politecnico di Milano has shown that the interference of wind tunnel walls in the NASA Glenn IRT does not greatly influence the final ice shape at the central station of the airfoil and so icing simulations can essentially be considered two-dimensional (Ref. 28). This however was tested based on a steady icing wind tunnel experiment and did not look further into three-dimensional effects introduced from unsteady flow fields. For simplicity and to ensure this analysis is within the scope of the timeline of the project the impending icing simulations are considered to be two-dimensional. This is also in agreement with the results obtained from the oscillating airfoil ice shapes which report little change along the spanwise direction although this is something that will require further investigation.

COMPUTATIONAL METHOD

The open-source SU2 software suite was used to determine the unsteady flow field over the oscillating airfoil (Ref. 29). The SU2 software suite solves partial differential equations on general unstructured grids. The core of the suite is a Reynolds-averaged Navier-Stokes solver which was used in this simulation in tandem with the Menter shear-stress transport turbulence model. Spatial discretization was achieved using an edge-based finite volume method. The convective and viscous fluxes are then evaluated at the midpoint of an edge. The Jameson-Schmidt-Turkel numerical scheme was used to solve the convective fluxes with a 2nd order limiter for the up-wind convective scheme. Whilst to evaluate the viscous fluxes using a finite volume method the Green-Guass numerical scheme was used. To account for the unsteady nature of the problem a 2nd order accurate dual-time-stepping approach was used to transform the unsteady problem into a series of steady problems. Each physical time-step was then solved consecutively for a fictitious time until converged to a steady-state problem. Volumetric rigid motion was used to account

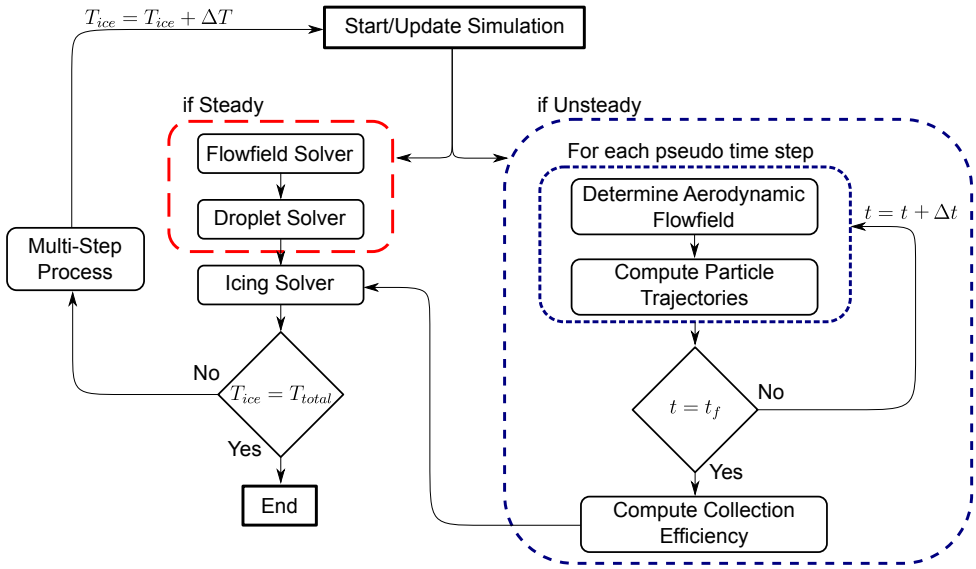

Fig. 1. Flowchart of the implementation of an ice accretion simulation. Displaying the different approaches for steady and unsteady flow field ice accretion simulations used in this work.

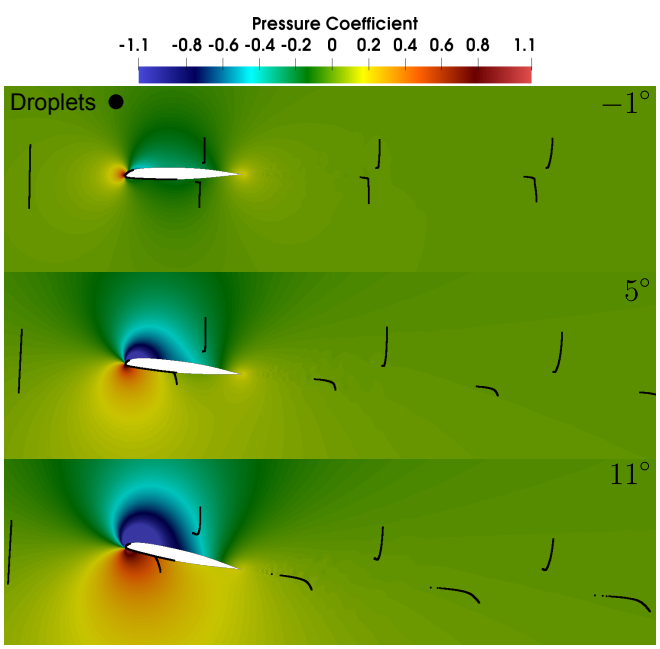

Fig. 2. Droplet trajectories in pressure flow fields at different instances in time as an airfoil oscillates.

for the sinusoidal movement of the oscillating airfoil where the whole grid rotates about a centred origin at each physical time-step. Convergence acceleration was achieved using an agglomeration multi-grid implementation to generate 4-levels of grid coarsening from the provided fine grid at run-time.

In-house codes PoliDrop and PoliMIce were used to respectively to determine the collection efficiency and final ice shapes (Ref. 30). The PoliDrop code is a Lagrangian based particle tracking code which uses previously computed flow field data to determine the particle trajectories and impingement locations. The code has been developed to account for moving boundaries present in unsteady problems. After computing the particle trajectories it calculates the value of the collection efficiency, β which can be thought of as the collected mass of particles on the impacted area divided by the mass of the total number of particles in the entire cloud and is given by

$$\beta = \frac{\frac{\sum_i^n N_i m_p}{V_c}}{\frac{\sum_i^n D_i m_p}{V_t}} \tag{2}$$

where m_p is the mass of the particles, N_n is the number of boundary faces impacted by particles, D_n is the number of droplets, and $V_{c,\,t}$ is the volume of the impacted cloud and total cloud respectively.

The PoliMIce software library provides state-of-the-art ice formation models. The model used in this work to capture the complex experimental ice shapes is the local exact solution of the unsteady Stefan problem for the temperature profiles within the ice layer in glaze conditions (Ref. 31). This model moves from Myers' formulation and includes an unsteady description of the heat diffusion problem within the ice layer and uses local values of the air temperature outside the boundary layer to compute the convective heat fluxes. Furthermore, it is able to account for the mass transfer between rime and glaze regions. The ice shapes are then computed using an unsteady multi-step approach, whereby, non-linear ice accretion is accounted for by iteratively updating the surface solution on which the ice accretes.

The clean and iced airfoil shapes are then subject to a computational aeroacoustic (CAA) analysis using the permeable-surface Ffowcs-Williams-Hawkings (FWH) formulation in SU2 (Ref. 32), in order to help predict the early stages on ice accretion during flight to aid in warning the pilot of ice

formation. The permeable FWH formulation allows fluid to flow through the fictitious surface Γ_p. Details of the flow field are then extracted and the noise source is then propagated to the far-field. This implementation is shown in the schematic from Figure 3. The computational domain is thus divided into two separate regions; the near-field CFD region, Ω_1 and the far-field CAA region, Ω_2. The permeable surface Γ_p can be described by the shape function, $f = 0$ where if $f < 0$ it is inside the surface and if $f > 0$ it is outside the surface. The position of the FWH lies $\frac{3}{4}$ chords length from the airfoil trailing edge. The position of the observer locations was chosen based on where noise would likely be perceived on a conventional main rotor/tail rotor helicopter, either under the main rotor directly or slightly forward or aft of it. Hence three different observer locations are used to assess the noise in the far-field at 10 chords length from the centre of the airfoil at 45°, 90° & 135° from the inflow direction.

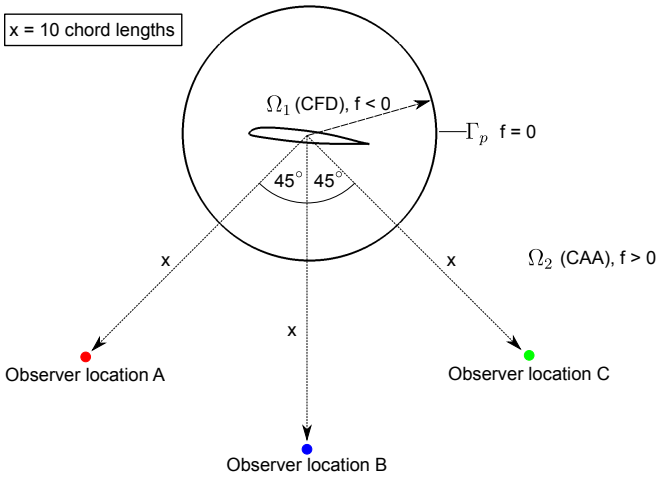

Fig. 3. Schematic of the permeable control surface Γ_p separating the CFD and CAA domains and the relative observer locations.

In accordance with the icing simulation, the acoustic analysis is likewise considered as a two-dimensional model, although it is understood the rotor blade noise is most definitely not two-dimensional in nature. It is for this reason, that this analysis is just for a proof of concept for the detection of different ice structure characterizations.

SPATIAL GRID CONVERGENCE

The surface node spacing of the mesh was determined through examining the spatial convergence of the coefficient of lift, C_L and the coefficient of drag, C_D. With the shape of the ice formation and thus the mesh structure unknown before the computation, the study was conducted on an un-iced airfoil. A constant angle of attack of $\alpha = 5°$ was used opposed to a sinusoidal oscillating motion so direct comparisons of C_L and C_D could be examined that would be time independent. Three levels of mesh refinement were assessed at a ratio of $r = 2$. The results of the mesh refinement on the C_L and C_D are shown in Table 2.

Table 2. Mesh refinement levels

Refinement Level	Surface Node Spacing (m)	r	C_L	C_D
1	0.00100	2	0.728955	0.011112
2	0.00050	2	0.725284	0.011036
3	0.00025	2	0.724400	0.011018

The Richardson extrapolation method (Ref. 33) was used for obtaining higher-order estimates of the continuum value at zero grid spacing, f_{exact} from a series of lower-order discrete values $(f_1,\ f_2,\ ..,\ f_n)$. The objective values used here were the C_L and C_D and as the grid spacing reduces they approach an asymptotic zero-grid spacing value which is assumed to be close to the true numerical solution.

The order of convergence, p can be obtained from three solutions using a constant grid refinement ratio, r and can be given as,

$$p = \ln\left(\frac{f_3 - f_2}{f_2 - f_1}\right) \ / \ \ln(r) \tag{3}$$

where the theoretical order of convergence is $p = 2$, however, this is not usually achievable due to the grid quality. The Richardson extrapolation can then be generalized by introducing the pth-order methods to solve for f_{exact} and to estimate the continuum value,

$$f_{exact} \cong f_1 + \frac{f_1 - f_2}{r^p - 1} \tag{4}$$

whilst the relative error, ε can be described as,

$$\varepsilon_{i+1,i} = \frac{f_{i+1} - f_i}{f_i} \tag{5}$$

The grid refinement error estimator derived from the theory of the generalized form of the Richardson extrapolation was then used to determine the Grid Convergence Index, *GCI* (Ref. 34). The *GCI* provides a measure of the percentage the computed value is away from the value of the asymptotic numerical value. The *GCI* and can be written as,

$$GCI_{i+1,i} = F_S \frac{|\varepsilon_{i+1,i}|}{r^p - 1} \tag{6}$$

where a factor of safety, $F_S = 1.25$ was used. The results of the spatial convergence analysis are shown in Table 3. There is a reduction in the *GCI* value for successive grid refinements for both the C_L and the C_D. It shows that during the first mesh refinement, from level $1 \rightarrow 2$, there is a significant difference compared to the asymptotic numerical solution, f_{exact}. During the second mesh refinement however, from level $2 \rightarrow 3$, the difference from the asymptotic numerical solution, f_{exact} is less.

With there being minimal difference between the $2 \rightarrow 3$ mesh refinements, and with the extra computational cost undesirable, the 2nd mesh refinement level was considered suitable and used for the subsequent computations. Thus, the mesh

Table 3. Grid Converence Index results

f	ε_{32}	ε_{21}	p	f_{exact}	GCI_{32}	GCI_{21}
C_L	1.22	5.04	1.94	0.724090	0.53%	2.21%
C_D	1.63	6.84	1.92	0.011011	0.73%	3.07%

contained a node spacing at the surface of the airfoil of 0.0005 m. The mesh then contained a cluster of finer cells close to the leading and trailing edges. The far-field was placed 14 chord lengths from the airfoil with a spacing of 0.05 m. The overall size of the mesh was 42,614 elements. A schematic of a close-up of the mesh around the clean airfoil is shown in Figure 4.

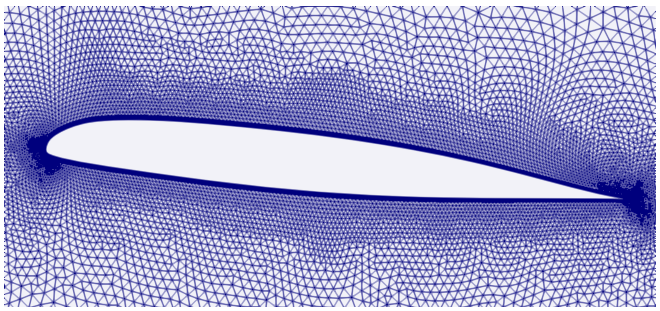

Fig. 4. Close-up of the mesh around the clean airfoil with 2-levels of surface mesh refinement.

NUMERICAL RESULTS AND DISCUSSION

A comparison between the computed ice shapes using the fully unsteady collection efficiency approach against experimental data and previously computed computational ice shapes will now be discussed. Due to there being no quantitative performance information found to be available about the Sikorsky SC2110 rotor airfoil during icing conditions the performance characteristics of the computed ice shapes will be compared against the performance characteristics of the computed un-iced airfoil. A visual explanation of these performance characteristics will then be aided with flow field diagrams showing the flow structure over clean and iced airfoils. Finally, an acoustic analysis at different monitoring points placed relative to the oscillating airfoil is shown.

1st Test Case - Run Number 36

Icing Analysis The first test case considered is run number 36 from the experimental work. This is considered to be the baseline test condition which all other flow fields and meteorological conditions are based on for the comparison of ice shapes. Run number 36 is a low flight speed case with a moderate value of LWC present during icing conditions. The results of the icing simulation of run number 36 are shown in Fig. 5. The simulated ice shapes produced from PoliMIce display a characteristic "spearhead" generated typically during rime ice conditions. The ice thickness appears moderate with slight asymmetry caused by the mean angle of attack. The experimental results show a rougher shape than the results computed from PoliMIce. The rough feather shapes were found to be very difficult to capture due to their large irregularities over the surface. The overall shape however appears to be in very good agreement with the experimental data. In particular agreement is the impingement limits of ice on the upper and lower surface of the airfoil. The IceMaker code from Boeing is used for code comparison with their quasi-static icing approach. The results from PoliMIce using the fully unsteady collection efficiency approach share many similarities with the results from IceMaker. Both codes however are unable to replicate the uneven ice profile and approximate smoothed curves opposed to the much rougher ice shape. This however is not of the greatest concern as the reproducibility of these uneven shapes would likely change from one experimental test to another.

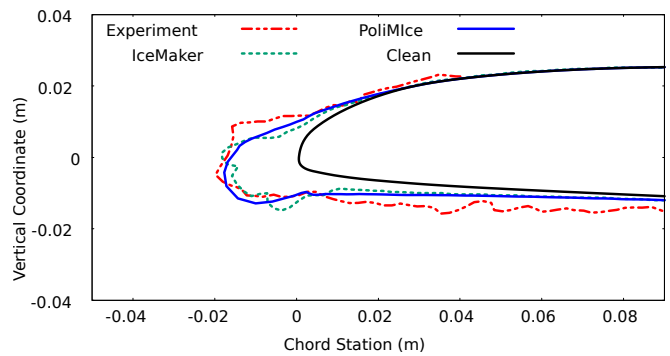

Fig. 5. Comparison of the experimental ice shapes and computed ice shapes from PoliMIce and IceMaker. The ice shapes are associated to run number 36.

Performance Analysis The prediction of the performance degradation caused from this ice shape is compared against the performance characteristics of a clean airfoil free of ice in Figures 6 & 7.

The first performance characteristic investigated is the lift coefficient of the oscillating airfoil shown in Figure 6. Immediately it is noticed how close the two lift hysteresis loop results correlate and in fact the iced airfoil increases the lift coefficient. This result can be explained by the fact that as the ice thickness increases the characteristic length used to compute the lift coefficient remains unchanged giving rise to an increase in lift. Furthermore, the smooth ice shape does not greatly disturb the airfoils flow characteristics. It also effectively increases the airfoil chamber which may slightly help at high angles of attack.

The second performance characteristic assessed is the moment coefficient of the oscillating airfoil shown in Figure 7. It is clear here that despite the lift coefficient remaining largely unaffected by the ice structure, the moment coefficient is affected quite severely by icing even with such aerodynamically acceptable ice shapes. At low angles of attack there is a stronger nose-up pitching moment and at high angles of attack there is a stronger nose-down pitching moment when in

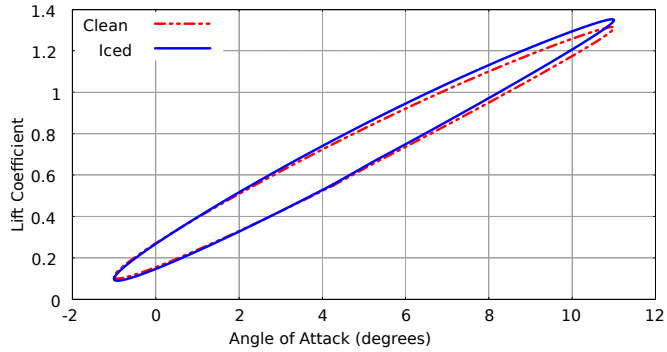

Fig. 6. Comparison of the predicted clean and iced airfoil lift coefficients. The iced airfoil refers to run number 36.

comparison with the clean airfoil moment characteristics. The thickness of the hysteresis loop also broadens compared to the thickens of the clean airfoil. Despite this, the moment hysteresis loops share the same profiles. These differences may be attributed to the ice increasing the chord and changing the location of the $\frac{1}{4}$chord at which the moment is computed. Although the increase in chord due to ice is slight it is clear that is has a significant effect on the moment coefficient.

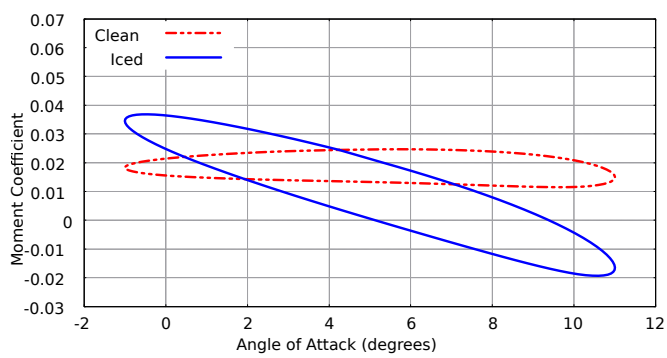

Fig. 7. Comparison of the predicted clean and iced airfoil moment coefficients from run number 36.

Flowfield Analysis The performance characteristics shown in Figures 6 & 7 can be further explained when examining the two flow fields of the clean and iced airfoils as depicted in Figure 9. The results from Figure 9 compare the clean and iced airfoils and display the velocity magnitude with spatially uniform streamlines at the minimum, median and maximum angles of attack. It shows that the ice shape from Figure 5 has very minimal effect on the flow field and as the flow passes over the leading edge of the iced airfoil at all angles of attack the flow remains attached downstream. The stagnation location is not affected and there is no flow separation from this ice shape. It is for this reason why the two observed performance characteristics of the clean and iced airfoils remain largely recognizable.

Acoustic Analysis The acoustic signals of clean and iced airfoils are shown in Figure 8. The perturbations in pressure, $p' = p_{\text{observer}} - p_\infty$ are shown at different observer location from the centre of the oscillating airfoil. These are shown over a time window long enough to display the noise sources periodicity. At all observer locations the rate of oscillation drives the harmonic frequency of the pressure perturbations. The magnitude of p' in all cases is significant to be detectable. At all observer locations there is a very slight increase in fluctuations in p' of the iced airfoil at the peaks of the waves and as the strength of the signal increases the difference in p' increases with it as shown at observer location B. Due to there being such similar flow characteristics between the clean and iced airfoils as shown in Figure 9 the noise signals are almost identical. Observer location B which is directly below the airfoil shows the strongest noise signals. Observer location A shows the next strongest noise signal and observer location C shows the weakest noise signal. Using these results as the difference in p' between the clean and iced increases with the magnitude of the fluctuations it would be sensible to place a noise detection system directly below the rotor to identify the rate of ice accretion.

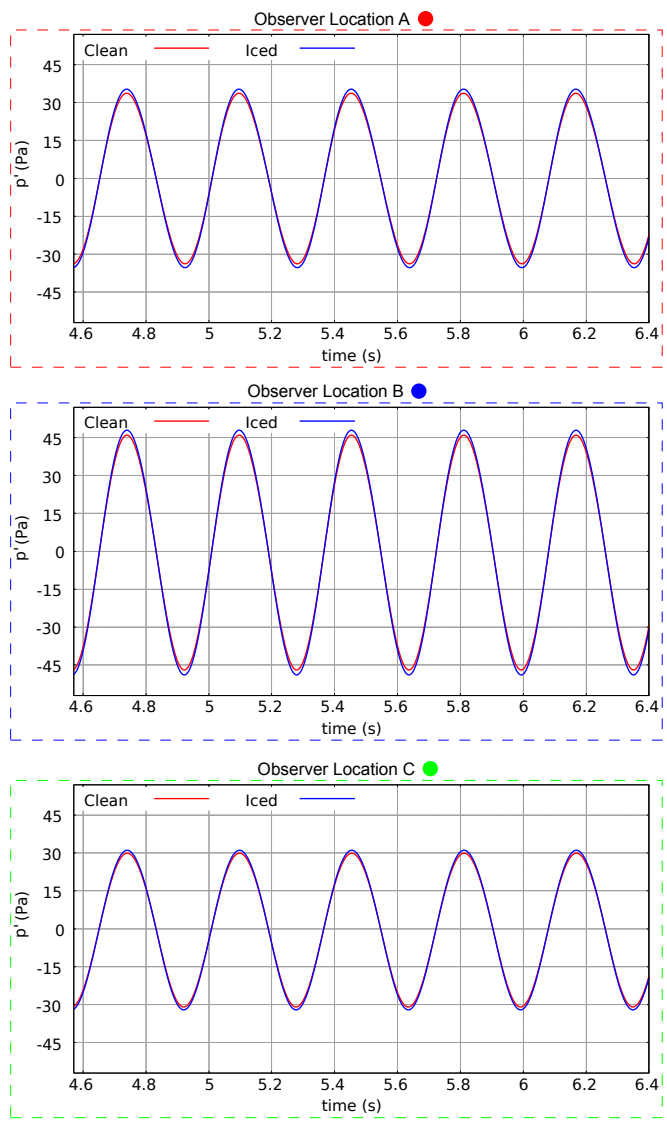

Fig. 8. Comparison of the predicted clean and iced airfoil acoustic signals. The iced airfoil refers to run number 36.

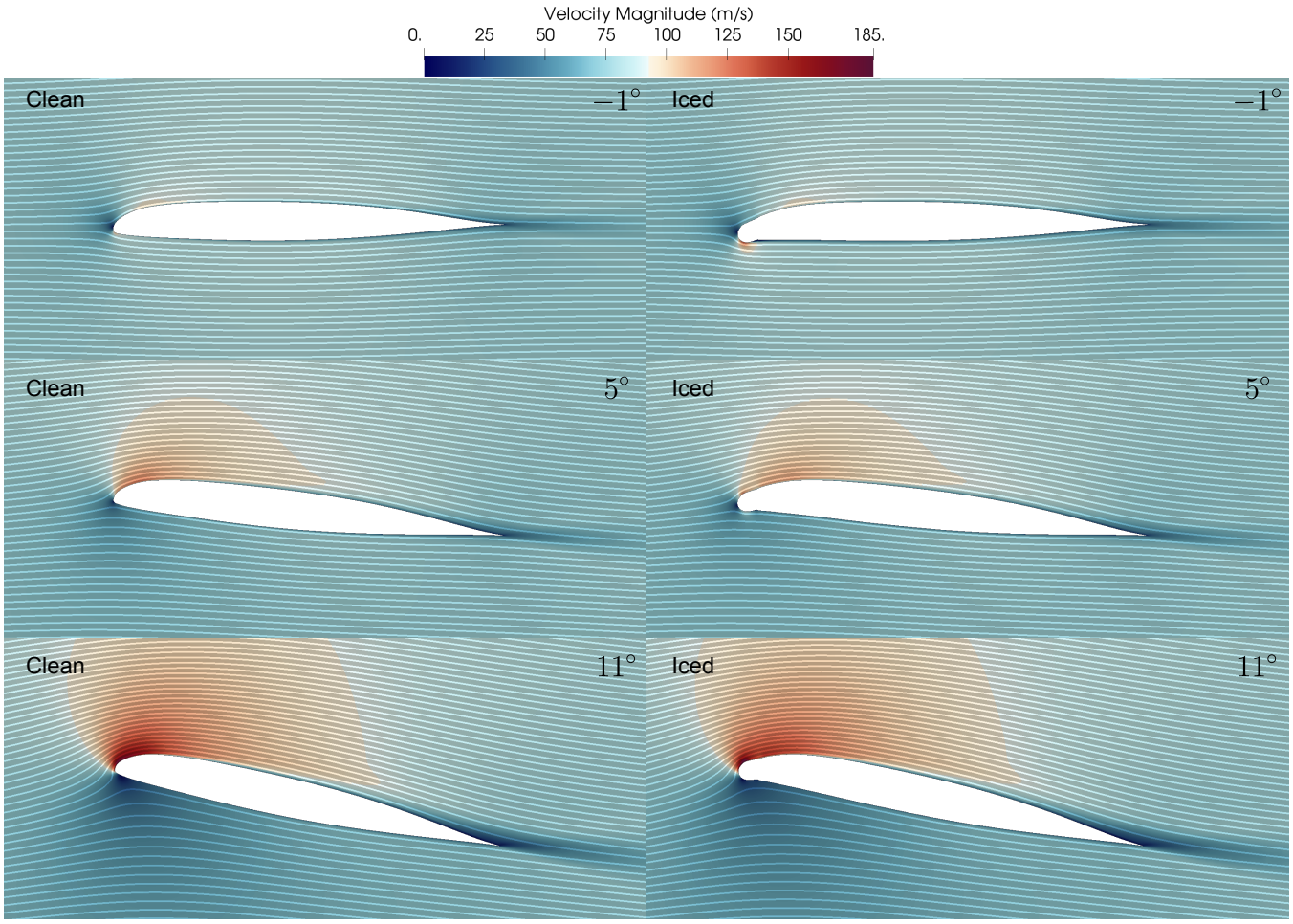

Fig. 9. Flow field comparison of the clean airfoil and the iced airfoil from run number 36. Diagram shows the velocity magnitude flow field and uniformly spaced streamlines across this flow field.

2nd Test Case - Run Number 61

Icing Analysis The second test case considered is run number 61 from the experimental database. This test case is identical to run number 36 except for a single environmental condition, the LWC. In this case there is a higher value of LWC at the upper scope of which would be expected in the meteorological environment. This means that the initial clean airfoil experiences the exact same flow conditions in both test cases and differences only arise after the first step of the multi-step ice accretion. Therefore, every droplet of supercooled water impacting on the airfoil contains a greater quantity of liquid water per cubic meter, resulting in, greater rates of ice accretion. The results of the icing simulation from run number 61 are shown in Figure 10 and produce distinct "double-horn" ice structures paradigmatic of mixed rime-glaze ice regimes. This was by far the most challenging of shapes simulated as it demands an ice accretion model which has an accurate account of local air temperature and the mass flux of liquid water from neighbouring cells. At the stagnation point the static air temperature is higher producing a large amount of liquid water which as it runs back accelerates and reaches areas of lower air temperature giving rise to the double-horn ice structure. The reason behind the double-horn ice structure being present here and not in run number 36 is due to there being less LWC per supercooled water droplet meaning there is less mass flux of liquid water between neighbouring cells and a lower rate of ice accretion. The ice shape results themselves are in good correlation with the experimental data especially the upper horn which is very closely reassembled. The lower horn is offset slightly, however, despite this the general shape is within good proximity to the experimental data. Similarly to the previous test case the computed ice shapes fail to capture the roughness of the ice. When the computed ice shapes are then compared against the prior computations from IceMaker they show a closer representation of the experimental ice shapes than IceMaker.

Performance Analysis The prediction of the performance degradation caused from this ice shape is compared against the performance characteristics of a clean airfoil free of ice in Figures 11 & 12.

The first performance characteristic investigated is the lift coefficient of the oscillating airfoil shown in Figure 11. Unlike the previous test case, the difference between the two results

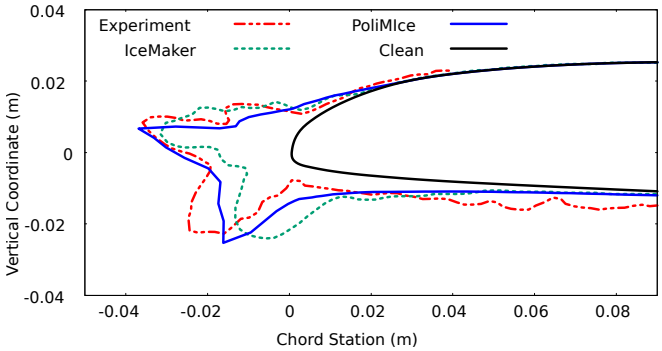

Fig. 10. Comparison of the experimental ice shapes and computed ice shapes from PoliMIce and IceMaker. The ice shapes are associated to run number 61.

is clear-cut and the lift coefficient hysteresis loops show little similarity. The iced airfoil depicts an airfoil experiencing dynamic stall as it approaches high angles of attack. On the upstroke of the oscillation, the lift coefficient is consistently less and as the airfoil reaches around 9° it experiences stall leading to a large reduction in lift. On the down-stroke, after the period of stall the lift coefficient settles as the flow reattaches and the lift coefficient reduces with the angle of attack. Here the increase in chord length appears insignificant compared the shape of the ice structure to increase the lift coefficient.

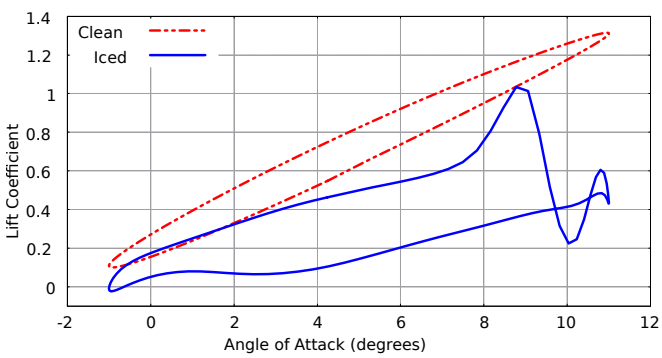

Fig. 11. Comparison of the predicted clean and iced airfoil lift coefficients. The iced airfoil refers to run number 61.

The second performance characteristic assessed is the moment coefficient of the oscillating airfoil shown in Figure 12. Immediately it is apparent the detrimental effect the ice shape has on the moment coefficient and in particular dynamic stall. On the upstroke of the oscillation, the moment coefficient fluctuates at a slight order of magnitude lower than the clean airfoil. As the airfoil reaches around 9° and stall occurs there is a severe peak in the moment coefficient causing a strong nose-up moment. On the down-stroke of the oscillation as the flow becomes reattached to the surface, the moment coefficient settles and again begins to fluctuate at a much lower order of magnitude. This dynamic effect would be extraordinarily difficult for pilots to handle.

Flowfield Analysis The performance characteristics shown in Figures 11 & 12 can be further explained when examining

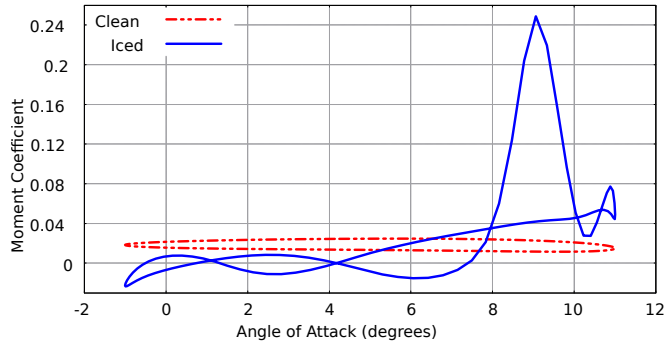

Fig. 12. Comparison of the predicted clean and iced airfoil moment coefficients from run number 61.

the two flow fields of the clean and iced airfoils as depicted in Figure 14. The results from Figure 14 compare the clean and iced airfoils and display the velocity magnitude with spatially uniform streamlines at the minimum, median and maximum angles of attack. It shows the severity the ice structure has on the flow field as it induces large amounts of flow separation causing dynamic stall. A stagnation point is present at the centre location of the two horns and as the flow moves downstream it is shown to accelerate around the horns. At the minimum angle of attack its shows that aft of the lower horn there is a strong vortex produced generating an area of chaotic flow. As the airfoils angle of attack increases the strength of the vortex aft of the lower horn decreases and the vortex aft of the upper horn strengthens. When the airfoil reaches the maximum angle of attack it shows complete flow separation from the airfoils upper surface causing the dynamic stall shown in the lift coefficient in Figure 11. The fluctuations in the moment coefficient in Figure 12 may be explained by the strengthening and weakening of the two vortices just aft of the upper and lower horns until high angles of attack when the large scale vortex on the upper surface dominates causing dynamic stall. It must however be acknowledged that due to the significant mesh distortion from the horn ice structure the spatial convergence of the numerical solution may no longer be applicable. To achieve spatial convergence of iced numerical solutions would require prior knowledge of the ice structure which is currently inconceivable.

Acoustic Analysis The time history of the pressure perturbations producing the noise signals of the clean and iced airfoils are shown in Figure 13. The fluctuations in p' of the iced airfoil in this case shows vastly different noise signals than to the clean airfoil. Once again the frequency of the oscillating airfoil drives the pressure fluctuations so there is clear periodicity present. The visibly different noise signals are attributed to be caused by the significant differences in the flow field as shown in Figure 14. On the upstroke of the iced airfoil the perturbations of p' show similar values to the clean airfoil. That is until the occurrence of the dynamic stall behaviour at which point large scale vortices are produced developing peaks of broadband noise at a magnitude far greater than the peaks of the clean airfoil noise signal. These peaks then begin to oscillate at a far higher frequency than the frequency

of the main noise signal. What is remarkable is the similarity between the high-frequency oscillations over each main oscillation. As with the previous test case the noise signal is strongest at observer location B directly below the airfoil. Observer location A then shows the next strongest signal and observer location C shows the weakest of signal although all three observer locations are at equal distances away from the airfoil. This supports the statement that if a noise detection system was used it should be placed directly below the rotor where the differences in clean and iced pressure perturbations are greatest.

The most significant finding here is the considerable difference between noise signal from the more aerodynamic ice shape from run number 36 and the catastrophically worse aerodynamic ice shape from run number 61. If ice shapes like that of run number 61 were to occur in-flight it is crucial the pilot quickly becomes aware of it due to the massively detrimental performance characteristics it causes. It is apparent from this work that if a relatively simple and low-cost noise detection system was in place it would be possible to detect which type of ice accretion was present on the surface in real time and the pilot would be able to react accordingly if the ice type shares similar ice shape characteristics to that from run number 61. This could be done by detecting large differences in the peak magnitude of the noise source or by detecting high-frequency noise sources associated to flow separation from horn ice structures.

CONCLUSION

An unsteady multi-step ice accretion method coupled with a fully unsteady collection efficiency approach is used here to aid in predicting ice shapes over an airfoil oscillating in an unsteady flowfield. The aerodynamics of the airfoil is modelled using an unsteady time accurate approach. The supercooled water droplets are transported within the unsteady flowfield and the airfoils moving boundaries are supported within the Lagrangian based particle tracking. The local solution of the unsteady Stefan problem was used to capture the complex experimental ice shapes. Ice shapes are then subject to a computational aeroacoustic analysis using the permeable-surface Ffowcs-Williams-Hawkings formulation. Experiments for the NASA Glenn IRT were used for comparisons of ice shapes. Overall some conclusions from this work can be drawn as follows:

1. The fully unsteady collection efficiency approach used to ensure unsteady aerodynamic effects are imposed on the supercooled water droplet trajectories helps predicts ice shapes very close to the experimental data and especially for mixed rime-glaze ice double-horn ice structures.

2. The contrast in the effect the ice structure has on the performance characteristics is observed, and mixed rime-glaze ice double-horn ice structure displays severe degradation in performance and the occurrence of premature on-set stall.

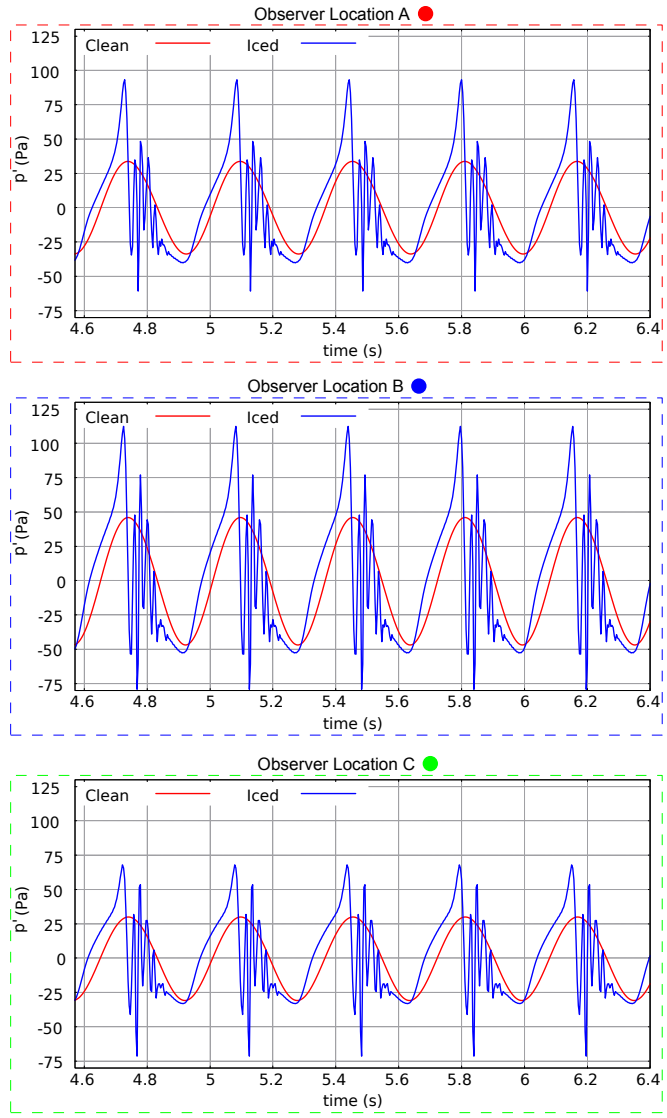

Fig. 13. Comparison of the predicted clean and iced airfoil acoustic signals. The iced airfoil refers to run number 61.

3. The acoustic analysis shows definite scope for the use of computational aeroacoustics to help detect different types of ice formation in real time for ice detection warning systems as the different cases produce recognizably different noise signatures. Looking ahead the use of machine learning (Ref. 35) on numerical data to train ice detection warning systems may be a suitable way forward.

This work focused on two different icing test cases for simplicity with the only variable being the value of the LWC in the supercooled water droplets which was differing. However, an array of other icing test cases have also been simulated with varying flight speeds, oscillating frequencies and mean amplitudes, and duration of icing times. These will then be subject to further analyses to draw additional conclusions about the role the ice shape has on the performance of the oscillating airfoil. With the inherent nature of rotor blades being largely dominated by three-dimensional flows the limitations of this

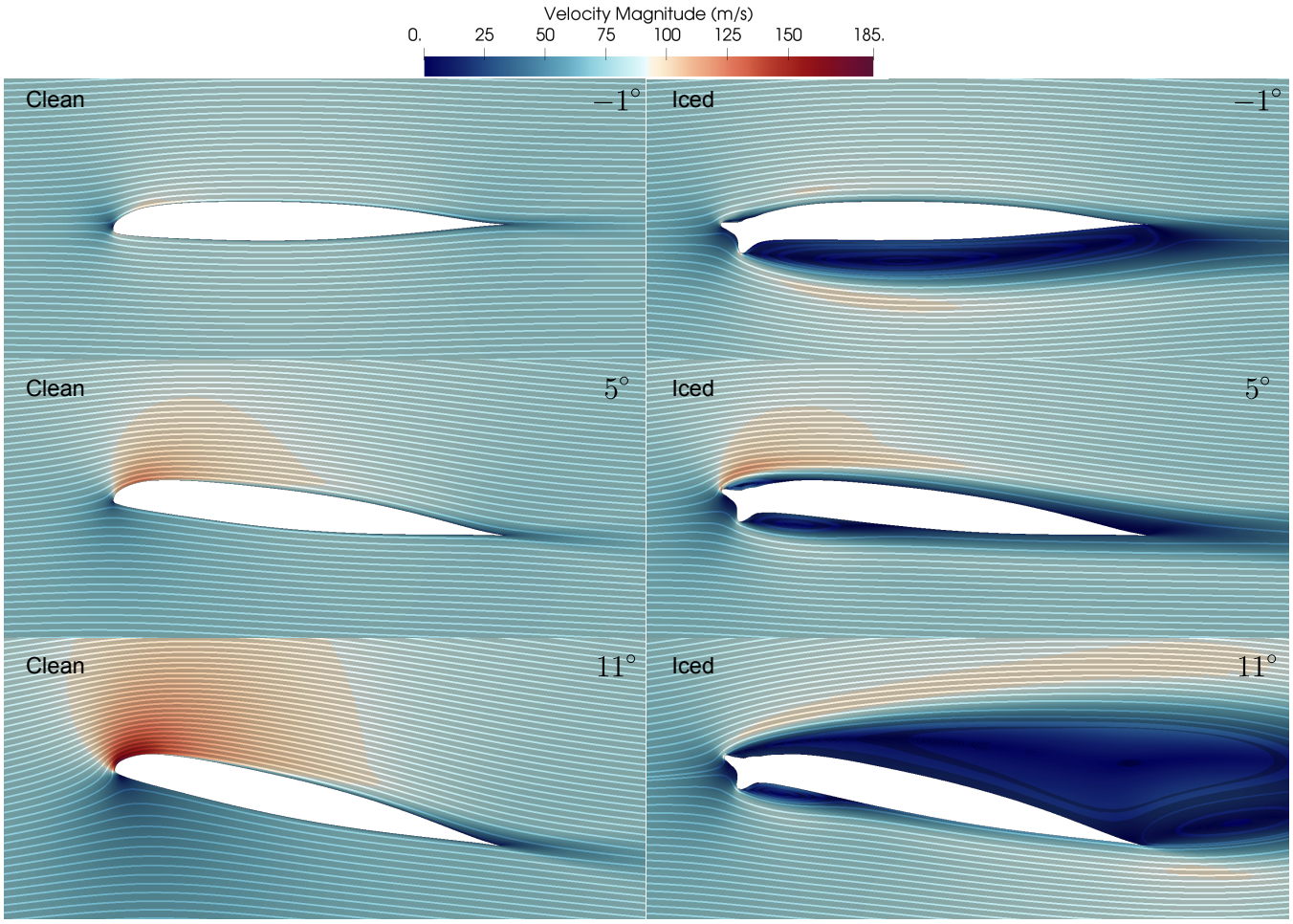

Fig. 14. Flow field comparison of the clean airfoil and the iced airfoil from run number 61. Diagram shows the velocity magnitude flow field and uniformly spaced streamlines across this flow field.

work are understood, however, the fundamental principals behind this study will remain intact for the future when this work is to be extended.

Author contact:

Myles Morelli – Email address: mylescarlo.morelli@polimi.it

ACKNOWLEDGEMENTS

This project has received funding from the European Unions H2020 research and innovation programme under the Marie Skodowska-Curie grant agreement No 721920. Further information can be found at the Network for Innovative Training on ROtorcraft Safety (NITROS) project website.

REFERENCES

[1]TEMSCO, "Air Ambulance Helicopter Operational Procedures," Temsco Helicopters Inc. Chapter IX, Revision 4, July 1997.

[2]EASA, "Type Certificate Data Sheet: Airbus Helicopters, AS 350/EC 130," EASA TCDS No.: EASA.R.008, March 2018.

[3]NTSB, "National Transportation Safety Board Aviation Accident Final Report," NTSB No. WPR17FA047, December 2017.

[4]NTSB, "National Transportation Safety Board Aviation Accident Final Report," NTSB No. WPR16LA104, June 2018.

[5]NTSB, "National Transportation Safety Board Aviation Accident Final Report," NTSB No. ANC16FA023, January 2018.

[6]NTSB, "National Transportation Safety Board Aviation Accident Final Report," NTSB No. ERA16LA167, October 2017.

[7]NTSB, "National Transportation Safety Board Aviation Accident Final Report," NTSB No. ERA15FA096, January 2017.

[8]NTSB, "National Transportation Safety Board Aviation Accident Final Report," NTSB No. WPR15FA072, October 2016.

[9]NTSB, "National Transportation Safety Board Aviation Accident Final Report," NTSB No. ERA15FA085, March 2017.

[10]EASA, "Easy Access Rules for Large Rotorcraft (CS-29)," EASA Amendment 4, June 2018.

[11]FAA, "Certification of Transport Category Rotorcraft," Adivisory Circular No: 29-2C, May 2014.

[12]Niemann, J. R., Bowers III, F. J., and Spring, S. C., "Artificial Icing Test CH-47C Helicopter with Fiberglass Rotor Blades." Army Aviation Engineering Flight Activity Edwards AFB CA, USAAEFA Project No.78-18, July 1979.

[13]Belte, D., "Helicopter Icing Spray System (HISS) Nozzle Improvement Evaluation," Army Aviation Engineering Flight Activity Edwards AFB CA, USAAEFA Project No.79-02-2, September 1981.

[14]Belte, D. and Woratschek, R., "Helicopter Icing Spray System (HISS) Evaluation and Improvement," Army Aviation Engineering Flight Activity Edwards AFB CA, USAAEFA Project No.82-05-3, April 1986.

[15]Lee, J. D., Harding, R., and Palko, R. L., "Documentation of ice shapes on the main rotor of a UH-1H helicopter in hover," NASA Report No.168332, January 1984.

[16]Miller, T. L. and Bond, T. H., "Icing research tunnel test of a model helicopter rotor," NASA Technical Memorandum No. 101978, May 1989.

[17]FLEMMING, R., BOND, T., and BRITTON, R., "Results of a sub-scale model rotor icing test," 29th Aerospace Sciences Meeting, January 1991.

[18]Tsao, J.-C. and Kreeger, R. E., "Evaluation of scaling methods for rotorcraft icing," NASA Technical Memorandum No. 215801, March 2010.

[19]Flemming, R., "The past twenty years of icing research and development at Sikorsky Aircraft," 40th AIAA Aerospace Sciences Meeting & Exhibit, January 2002.

[20]Flemming, R. J., Britton, R. K., and Bond, T. H., "Role of wind tunnels and computer codes in the certification and qualification of rotorcraft for flight in forecast icing," NASA Technical Memorandum No. 106747, October 1994.

[21]Reinert, T., Flemming, R. J., Narducci, R., and Aubert, R. J., "Oscillating Airfoil Icing Tests in the NASA Glenn Research Center Icing Research Tunnel," SAE Technical Paper No. 2011-38-0016., June 2011.

[22]Fortin, G. and Perron, J., "Spinning rotor blade tests in icing wind tunnel," 1st AIAA Atmospheric and Space Environments Conference, June 2009.

[23]Bain, J., Sankar, L. N., Aubert, R. J., and Flemming, R. J., "A methodology for the prediction of rotor blade ice formation and shedding," SAE Technical Paper No. 2011-38-0090, June 2011.

[24]Narducci, R. and Reinert, T., "Calculations of Ice Shapes on Oscillating Airfoils," SAE Technical Paper No. 2011-38-0015, June 2011.

[25]Kreeger, R. E., Sankar, L., Narducci, R., and Kunz, R., "Progress in Rotorcraft Icing Computational Tool Development," SAE Technical Paper No. 2015-01-2088, June 2015.

[26]Cheng, B., Han, Y., Brentner, K. S., Palacios, J. L., and Morris, P. J., "Quantification of rotor surface roughness due to ice accretion via broadband noise measurement," American helicopter society 70th annual forum proceedings, 2014.

[27]Carr, L. W., McAlister, K. W., and McCroskey, W. J., "Analysis of the development of dynamic stall based on oscillating airfoil experiments," NASA Technical Note D-8382, January 1977.

[28]Zocca, M., Gori, G., and Guardone, A., "Blockage and Three-Dimensional Effects in Wind-Tunnel Testing of Ice Accretion over Wings," *Journal of Aircraft*, Vol. 54, (2), April 2016, pp. 759–767.

[29]Economon, T. D., Palacios, F., Copeland, S. R., Lukaczyk, T. W., and Alonso, J. J., "SU2: An open-source suite for multiphysics simulation and design," *AIAA Journal*, Vol. 54, (3), December 2015, pp. 828–846.

[30]Gori, G., Zocca, M., Garabelli, M., Guardone, A., and Quaranta, G., "PoliMIce: A simulation framework for three-dimensional ice accretion," *Applied Mathematics and Computation*, Vol. 267, September 2015, pp. 96–107.

[31]Gori, G., Parma, G., Zocca, M., and Guardone, A., "Local Solution to the Unsteady Stefan Problem for In-Flight Ice Accretion Modeling," *Journal of Aircraft*, Vol. 55, (1), 2017, pp. 251–262.

[32]Zhou, B. Y., Albring, T., Gauger, N. R., Ilario, C. R., Economon, T. D., and Alonso, J. J., "Reduction of Airframe Noise Components Using a Discrete Adjoint Approach," AIAA-2017-3658, 2017.

[33]Richardson, L. F. and Gaunt, J. A., "VIII. The deferred approach to the limit," *Philosophical Transactions of the Royal Society of London. Series A, containing papers of a mathematical or physical character*, Vol. 226, (636-646), 1927, pp. 299–361.

[34]Roache, P. J., "Perspective: a method for uniform reporting of grid refinement studies," *Journal of Fluids Engineering*, Vol. 116, (3), 1994, pp. 405–413.

[35]Soize, C., Ghanem, R., Safta, C., Huan, X., Vane, Z. P., Oefelein, J. C., Lacaze, G., and Najm, H. N., "Enhancing Model Predictability for a Scramjet Using Probabilistic Learning on Manifolds," *AIAA Journal*, Vol. 57, (1), 2018, pp. 365–378.